Variable fault geometry suggests detailed fault slip rate profiles and geometries are needed for fault-based probabilistic seismic hazard assessment (PSHA)

J.P. Faure Walker[1], F. Visini[2], G. Roberts[3], C. Galasso[4], K. McCaffrey[5], Z. Mildon[1,6]

[1] Institute for Risk & Disaster Reduction, University College London

[2]Istituto Nazionale di Geofisica e Vulcanologia

[3]Department of Earth and Planetary Sciences, Birkbeck College

[4]Department of Civil, Environmental & Geomatic University College London

[5]Department of Earth Sciences, Durham University, Science Labs,

[6] now at Centre for Research in Earth Sciences, University of Plymouth

Abstract

It has been suggested that a better knowledge of fault locations and slip rates improves seismic hazard assessments. However, the importance of detailed along-fault slip rate profiles and variable fault geometry has not yet been explored. We quantify the importance for modeled seismicity rates of using multiple throw rate measurements to construct along-fault throw rate profiles rather than basing throw rate profiles on a single measurement across a fault. We use data from 14 normal faults within the central Italian Apennines where we have multiple measurements along the faults. For each fault, we compared strain rates across the faults using our detailed throw rate profiles and using degraded data and simplified profiles. We show the

implied variation in average recurrence intervals for a variety of magnitudes that result. Furthermore, we demonstrate how fault geometry (variable strike and dip) can alter calculated ground shaking intensities at specific sites by changing the source-to-site distance for ground motion prediction equations (GMPEs). Our findings show that improved fault-based seismic hazard calculations require detailed along-fault throw rate profiles based on well-constrained local 3D fault geometry for calculating recurrence rates and shaking intensities.

Key Words

Earthquake, fault, seismic hazard, recurrence intervals, geometry, PSHA, GMPEs, Apennines

Introduction

Active fault locations and slip rates are the principal controls on earthquake locations and time-averaged recurrence rates, but fault data are currently under used within hazard assessments used to calculate earthquake risk. The need for long-term fault-derived slip rates for probabilistic seismic hazard assessment (PSHA) has been noted (*e.g. Faure Walker et al., 2010; Stein et al., 2012; Papanikolaou et al. 2015; Blumetti et al., 2017*). In particular, multi-millennia fault slip rates provide an opportunity to capture a long-term record of cumulative earthquake displacements covering multiple seismic cycles and avoiding the bias introduced by temporal earthquake clustering. From this average recurrence intervals can be inferred for individual faults. Some researchers are incorporating long-term fault slip rates into hazard models for different regions of the world (e.g. California, USA: *Field et al., 2014*; Italy: *Valentini et al., 2017*; Greece: *Deligiannakis et al., 2018*) and tools have been developed to help researchers with

such endeavors (e.g. FiSH, *Pace et al., 2016*). However, fault slip rates remain one of the key uncertainties in calculating earthquake probabilities (*Field et al., 2014*) and the lack of detailed and accurate fault slip rate data necessitates making assumptions regarding how to propagate data collected at a single site along the length of the fault.

The problem of propagation of data along strike is clearly important, because what is known from multi throw rate and slip rate measurements along single faults is that they are highly variable; however, current fault-based approaches for calculating earthquake hazard do not incorporate these detailed variations. Instead they use along-strike throw rate or slip rate profiles with artificially assigned simplified shapes extrapolated from one to a few measurements along simplified planar faults. This is in some ways inevitable because more detailed data are rarely available (e.g. *Field et al.*, *2014*). However, detailed data are available for active normal faults (e.g. *Cartwright and Mansfield, 1998; Contreras et al., 2000; Faure Walker et al., 2009; 2010; 2015; McClymont et al., 2009; Wilkinson et al., 2015; Mildon et al., 2016a; Reilly et al., 2016*) and this prompts the present study where we explore the effect of along-strike throw rate variability for seismic hazard. Fortunately, locations where throw rates vary dramatically along the strike of individual faults may be easy to identify, because along-strike profiles of throw rates on active faults are altered where faults show non-planar fault geometry (*Faure Walker et al., 2009; 2015*). Additionally, the reasons for the throw rate variations are well-understood due to development of quantitative relationships between throw rate and fault geometry (*Faure Walker et al., 2009; 2015; Wilkinson et al., 2015; Mildon et al., 2016a; Iezzi et al., submitted*). Specifically, throw rates are increased across bends in faults so that the strain rates across the fault remain concomitant with their position along the fault (Figure 1). The geometry-dependent throw rate model suggests active normal faults have local throw rates governed by a combination

of regional-scale external forces, displacement gradients along faults, and local 3D fault geometry which are inter-related (*Faure Walker et al., 2009)*. The model may further explain much of the scatter and variations in shape of along fault displacement profiles (e.g. *Manighetti et al., 2005*) and the scatter seen in maximum slip against rupture length graphs of *Wells and Coppersmith (1994)* (*Iezzi et al., submitted*). In this paper we demonstrate the effect of spatial variations in throw rate along individual faults for implied average recurrence intervals.

Another factor that has not been demonstrated is the compounded impact of including detailed fault geometry and throw rate measurements for calculating modeled shaking intensities. These will change because along-strike bends in the map traces of faults change the distance to sites where shaking intensity is of interest; where brought closer to the fault, the intensity will increase and the recurrence time will decrease due to higher slip rate, compounding the threat. We emphasize that shaking intensities at given locations are a critical input for earthquake risk assessment - the first step towards the development of risk reduction strategies - and performance-based earthquake design. For instance, the design peak ground acceleration (PGA) value for the 'ultimate limit state' or ‘life-safety’ performance objective is typically based on the annual rate of exceedance of 1/475 (corresponding to a mean return period of 475 years) (e.g., the current Italian Building Code, or IBC08, see *Iervolino et al., 2011*) and this will be affected by distance to the fault traces that rupture. This is because GMPEs, also known as ground-motion models and attenuation relations, are typically used to model the intensity of shaking at individual sites and across an area, within the framework of PSHA. GMPEs are empirical models estimating the probability distribution of ground-motion intensity measures (IMs) - such as PGA and SA (spectral acceleration) - occurring at a given site as a function of magnitude, source-to-site distance between the seismic source (the fault) and the site of interest, soil properties at the

site, focal mechanism, and other parameters (e.g. *Bindi et al., 2011*). The source-to-site distance can be measured using a variety of metrics, such as R_{jb} ("Joyner-Boore" distance), R_{rup} (slant distance), R_{cent} (centroid distance), R_{hyp} (hypocentral distance), and R_{epi} (epicentral distance), see for instance *Bommer and Akkar (2012)*. To be computed in practice and be used in hazard assessments, these metrics require knowledge of the fault location and dip. For example, R_{jb}, is the closest horizontal distance from the site to the vertical projection of the rupture surface, which is dependent on the surface trace of the fault and the dip of the fault. Even if most modern GMPEs use definitions of the source-to-site distance that reflect the dimensions of the fault rupture for larger earthquakes rather than using point-source measures relative to the epicenter or hypocenter, the role of variable fault strike and a change of dip along strike are generally not considered in GMPEs used for hazard calculations or in the other steps of PSHA. In this paper we show that detailed knowledge of strike-variable fault geometries changes calculated shaking intensities, a critical input for PSHA.

The background to our emphasis on using detailed fault slip rate and fault geometry data is that most seismic hazard models currently used by government civil protection agencies to inform building codes and emergency planning, and by the (re)insurance industry, are driven by historical earthquake data and by the definition of seismic source zones, or areal sources, i.e., all the points within the considered area can be the epicenter of earthquakes with the same probability (e.g. *Stucchi et al.*, *2011*). This is in spite of it being known that historical and seismological records are of insufficient length relative to average fault recurrence intervals to be representative of longer time periods and capture the geography of seismic hazard (e.g. *Camelbeeck et al., 2007; Stein et al., 2012; Liu and Stein, 2016; Blumetti et al., 2017*). In particular, in continental settings, faults exist that are capable of producing large magnitude

earthquakes that have not ruptured in historical times (e.g., *Liu et al., 2011; Mildon et al., 2017; Hintersberger et al. 2018*). For instance, in the central Apennines, Italy, the historical records are restricted to hundreds of years, but individual faults have recurrence intervals of hundreds to thousands of years (e.g. *Pace et al., 2006; Galli et al., 2008*). In August and October 2016, three earthquakes Mw 5.9 - 6.5 ruptured the Mt. Vettore fault (e.g. *Livio et al., 2016; Cheloni et al., 2017; Pucci et al., 2017; Civico et al., 2018; Villani et al., 2018*), a known active mapped fault that had not ruptured within the historical record but had clear evidence of meter-scale Holocene slip events (*Galadini and Galli, 2003; Mildon et al., 2017*; *Wedmore et al., 2017*). PSHA based on the historical record prior to these events would not explicitly include the hazard from this fault, or others that have not ruptured during historical times. Other examples worldwide such as the 2011 Great East Japan Earthquake and the 2010 Haiti Earthquake have had their probability underestimated because the fault displacement rates were not properly considered (*Stein et al., 2012*). At a scale larger than individual faults, the pitfalls of using only shorter-term historical and seismicity data or deformation rates derived from geodesy to infer hazard have been highlighted in continental settings such as the central Italian Apennines *(Faure Walker et al., 2010)* and North China (*Liu et al., 2011*). For example, in the central Italian Apennines, calculated long-term (15±3kyr) fault-derived strain rates in polygons with areas in the order of 1,000km^2 do not match short-term strain rates inferred from historical moment tensors (700yrs) and geodesy (126yrs) (*Faure Walker et al., 2010*). The short-term (700yr) strain rates are lower than long-term (15±3kyr) strain rates in some areas but higher in others (*Faure Walker et al., 2010*). This leads to dramatic underestimations and overestimations of hazard for those areas respectively if calculated solely from historical records (*Faure Walker et al., 2010*). Without the longer-term view, hazard assessments will continue to be biased by the most recent events and

hence risk from faults that have not ruptured in recent or historical times will not be communicated (e.g. *Liu and Stein, 2016*).

In this paper, we first calculate strain rates and average recurrence intervals for a fault where data on detailed along-strike variations in throw rate are available, and then demonstrate how degrading detailed along-strike throw rate profiles to simplified idealized along-strike throw rate profiles affects the calculated strain rate across a single fault. We then expand this investigation to 14 individual faults for which we have moderately detailed data. For our example fault we show how the simplifications to the throw rate profile affect average recurrence intervals calculated using FiSH software (*Pace et al., 2016*). For another example fault, we investigate the effect of simplifying fault map geometry and throw rate profiles on expected shaking intensities. We find that detailed fault throw rate profiles and fault geometries can have significant impact on calculated recurrence rates and ground shaking intensities at specific sites. Therefore, we argue that such variations should be considered within uncertainties of fault-based probabilistic seismic hazard assessments.

Geological Background

The studied faults are located in the central Apennines, Italy, a region of extending continental crust where offset 15±3ka landforms and sediments can be used to constrain throw rates across normal faults (Figure 2) (e.g. *Piccardi et al., 1999; Roberts and Michetti, 2004*). Evidence for the age of the offset landforms and sediments comes from tephrachronology, ^{36}Cl cosmogenic exposure dating of fault scarps and upper slopes, the timing of a change from periglacial processes dominating slopes along active faults to slopes controlled by surface fault slip, and shifts in $\delta^{18}O$ from Tyrrhenian and other Mediterranean sea cores (*Giraudi and*

159 *Frezzotti, 1986; Giraudi & Frezzotti, 1997; Allen et al., 1999; Cowie et al., 2017*). Average
160 15±3ka fault throw rates can be derived from topographic profiles across the offset slopes (e.g.
161 *Roberts and Michetti, 2004*). This time period covers multiple seismic cycles (e.g. *Palumbo et*
162 *al., 2004; Galli et al., 2008; Cowie et al., 2017*). 15ka throw rates are representative of even
163 longer time periods demonstrated by calculated strain rates averaged over 15±3ka correlating
164 with total fault throws across the faults developed since 2-3Ma, mantle SKS splitting delay
165 times, and elevation above sea-level via a power law with exponent ~3 (*Faure Walker et al.,*
166 *2012; Cowie et al., 2013*). This supports the idea that average recurrence intervals derived from
167 15±3ka rates are stable for even longer time periods. A map of the active faults in the region is
168 shown in Figure 3 with the 14 faults investigated in this study highlighted.

169

170 **Methods**

171 We show the relevance for earthquake hazard calculations of using detailed or degraded data
172 for a single fault, and then for 14 studied normal faults in the central Italian Apennines. We
173 calculate strain rates across each of these faults using detailed measurements of fault strike, dip
174 and throw rate. We compare the results to strain rates calculated across the same 14 faults, but
175 assuming planar fault geometry and taking a single measurement of the throw rate and using this
176 value to create assumed, simplified along-strike throw rate profiles assuming either a 'boxcar' or
177 'triangular' profile (examples shown in Figure 4b). Using an example fault for each, we compare
178 the detailed and degraded data cases for modeled average recurrence intervals and annual rates of
179 exceeding specified ground shaking intensities.

180 Previously published data, supplemented by new fieldwork data (Table 1), of fault throws,
181 and slip vector azimuths and plunges were used for the fault geometry, slip vectors and throw

rates needed as inputs to strain rate calculations (Figure 2) (*Morewood and Roberts, 2000; Roberts and Michetti, 2004; Papanikolaou et al., 2005; Papanikolaou and Roberts, 2007; Faure Walker et al., 2009; 2010; 2012; Wilkinson et al., 2015; Cowie et al., 2017; Mildon, 2017; Wedmore, 2017*). The selected faults were mapped using field mapping, digital elevation models, satellite imagery, SRTM (Shuttle Radar Topography Mission) data, geological maps and paleoseismic trench data (*Roberts and Michetti, 2004; Roberts, 2008; Faure Walker et al., 2009; 2010; 2012; Cowie et al., 2017*). Topographic profiles across exposed fault scarps constraining the throw rate at multiple sites along the faults have been constructed using slope angles measured directly in the field (Figure 2, see *Faure Walker et al., 2010* for a review of the method). At selected sites topography profiles have been extracted from DEMs constructed from terrestrial LiDAR scanning (see *Wilkinson et al., 2015* and *Cowie et al., 2017* for a review of the method). Slip vectors were determined by averaging measurements of multiple slickensides at each site on the exposed limestone fault planes (Figure 2).

The strain rate across each of the 14 individual faults was calculated building on methods developed by *Faure Walker et al. (2009, 2010)*. The method combines measurements of fault strike, dip, throw, length and slip vector azimuth and plunge to calculate moment tensors using adaptations of the *Kostrov (1974)* equations. To capture the local variations in fault geometry and throw rates, we discretized each non-planar fault on a regular grid with individual grid boxes having dimensions of 1km x 2km and calculated strain rates on planar segments confined within each grid box. For the strain rate across each whole fault (which vary in length between 5.5km and 46km) we combine grid squares to model the non-planar fault.

For each of the 14 studied faults we have at least four measurements of throw (one fault has 30 measurements while the remaining 13 faults have eleven or less) to contribute to the detailed

or ‘all data’ case. We remove data points for the degraded data cases. For example, for the Parasano-Pescina fault, we have seven data sites along the fault with values for the 15ka throw, geometry (strike and dip) and slip-vector (Figure 4a). To investigate the effect of using degraded data, we compare calculations of strain rate across this fault using (i) all data sites in the ‘all data’ throw profile with degraded data: (ii) leaving out the maximum throw point in the ‘no max’ profile but including the other measurements; (iii-) extrapolating a single throw along the whole fault in a ‘boxcar’ profile; and (iv) extrapolating throw along the fault by decreasing the maximum throw linearly to the fault tips in a ‘triangular’ profile (Figure 4b,c). We present three ‘boxcar’ scenarios: (iii-1) ‘boxcar-max’ which extrapolates the maximum throw along the whole fault; (iii-2) ‘boxcar-mean’ for which we integrate the throw profile to find the average displacement and extrapolate this along the whole fault; and (iii-3) ‘boxcar-min’ for which we extrapolate the minimum measured throw along the whole fault. For cases (i) and (ii) we use the detailed fault geometry, but for cases (iii) and (iv) we assume a planar fault geometry. We calculate strain rates across a further 13 faults for the ‘all data’, ‘boxcar-max’, ‘boxcar-mean’, ‘boxcar-min’ and ‘triangular’ throw profiles.

To demonstrate the effect of using degraded data for calculating earthquake rates, we calculate recurrence intervals for two of the faults: the Parasano-Pescina Fault and the Pescasseroli fault. The earthquake magnitude-frequency distributions have been modeled with a truncated Gutenberg-Richter relationship using the FiSH software (*Pace et al., 2016*). In this distribution, the *b*-value describes how the number of events with magnitude $\geq M$, N, changes with magnitude up to a threshold magnitude, above which N decreases more rapidly (*Kagan, 2002; Jackson & Kagan; 2006*). For this study, *b* is assumed to be 1 (following *Bird and Kagan, 2004; Valentini et al., 2017*). The maximum earthquake magnitudes (*Mmax*) of the truncated

228 Gutenberg-Richter relationship for each fault have been calculated using empirical relationships
229 based on fault length (*Wells and Coppersmith, 1994*).

230 To calculate activity rates at magnitudes given by the truncated Gutenberg-Richter
231 relationship, we balanced the expected seismic moment rate of the truncated Gutenberg-Richter
232 relationship with the seismic moment rate obtained by geometry and slip rates ($\dot{M}_g$):

233 $$M_g = \dot{\mu} LWV \qquad (1)$$

234 where μ is the shear modulus, V is the slip rate, and L and W are along-strike rupture length
235 and downdip width, respectively. In this study, to include slip rate variability along strike, as
236 well as detailed slip rate profiles, we assumed:

237 $$M_g = \mu \sum L_i W_i V_i \qquad (2)$$

238 where i indicates data of along-strike segments of a fault.

239 The effect of using degraded data on expected ground shaking at individual sites was
240 investigated through a site-specific PSHA. We calculate annual rates of exceeding specified
241 ground shaking intensities at a specified site. Earthquake rates for different earthquake
242 magnitudes are calculated as described above using the 'all data', 'boxcar-max' and 'triangular'
243 throw profiles. Shaking intensities for given magnitudes are calculated using GMPEs.

244 We use the widely-applied GMPEs for Italy (*Bindi et al., 2011*) to calculate the ground
245 shaking from earthquakes on the Pescasseroli fault at a given site several kilometers from the
246 fault. These GMPEs are derived for the geometrical mean of the horizontal components and the
247 vertical, considering the latest release of the strong motion database for Italy. The regressions are
248 performed over the magnitude range 4–6.9 and considering distances up to 200 km. The
249 equations are derived for PGA, peak ground velocity (PGV) and 5%-damped spectral

250 acceleration (SA) at periods between 0.04 and 2 s.

251 To test the effect of using simplified fault geometries on expected ground shaking intensities,
252 we compare the GMPE results basing the source-to-site distance on detailed fault geometry and
253 simplified planar fault geometries. Consistent with the used GMPEs, we use the R_{jb} source-to-
254 site distance. For the 'all data' throw profile, we use R_{jb} based both on detailed fault geometry
255 and simplified planar geometries. The simplified geometries use a planar fault strike projected
256 between the two fault tips and two different fault dips: one using the fault dip measured at the
257 site of maximum throw and the other using the fault dip measured at the fault tip. For the
258 'triangular' and 'boxcar-max' throw-profiles, the two planar fault geometries are modeled.

259 We account for uncertainty in the factors affecting ground motions by using a Monte Carlo
260 simulation-based approach (e.g. *Assatourians and Atkinson, 2013*). To this aim, a 10,000yrs
261 synthetically generated set of potential earthquakes across the Pescasseroli Fault, with their
262 temporal distribution, is developed by drawing random samples from the assumed PSHA model
263 components (and related probability distributions), i.e., magnitude-recurrence parameters and
264 maximum magnitude, as defined above. 500 realizations of random numbers drawn from the
265 standard normal distribution is multiplied by the given sigma value (variability of the GMPE
266 model) and added to the median log-ground motions (from the GMPEs) to model the aleatory
267 variability in ground motions. Site-specific hazard curves are displayed showing annual rates of
268 exceedance against PGA and SA(1s). For the 'all data' throw profile with the strike-variable
269 fault geometry, we show hazard curves of the PGA for each realization as well as the median,
270 16^{th} and 84^{th} curves (representing $\pm 1\sigma$). For all the simplified cases only the median curve is
271 shown. In general, SA(1s) can be used as good predictor of the structural response and induced-
272 damage of low-to-mid rise buildings, one of the most common construction types in Italy (e.g.,

273 *Rosetto et al., 2016*).

274

275 **Results**

276 The strain rates within individual 1km x 2km grid boxes across the Parasano-Pescina fault are
277 shown in Figure 4. Figure 4(i) shows the strain rates calculated using all the data. Figures 4(ii-iv)
278 show how the calculated strain rates across the whole fault change for the 'no max', 'boxcar-
279 max', 'boxcar-mean', 'boxcar-min' and 'triangular' throw profiles to 93%, 158%, 104%, 61%
280 and 78% of the 'all data' profile respectively (the bars and errors of the 'all data' case are shown
281 on each graph). The strain rates calculated across the fault using the 'boxcar-max' (iii-1),
282 'boxcar-min' (iii-3) and 'triangular' (iv) throw profiles are outside the error margins of the
283 calculated strain rate across the fault using all the available data (i).

284 In Figure 5, the calculated strain rates for the 'all data', 'boxcar-max', 'boxcar-mean',
285 'boxcar-min' and 'triangular' throw profiles are compared for each of the 14 studied faults. The
286 strain rates for each fault are normalized to the 'all data' case to allow comparison between the
287 calculated strain rate and the scenarios modeled with simplified throw rate profiles. For the
288 simplified 'boxcar-max', 'boxcar-mean', 'boxcar-min' and 'triangular' throw profiles, only one,
289 nine, two and three of the faults have strain rates within the 'all data' case errors respectively
290 (errors for strain rates across entire faults using 'all data' vary between 6% and 20%). Strain
291 rates across faults for the simplified cases vary from 51% to 303% relative to the 'all data' cases
292 and half of them have calculated strain rates <0.5 or >1.5 times the 'all data' cases. The results in
293 Figures 4 and 5 demonstrate that one measurement of throw extrapolated along strike in either a
294 'boxcar' or 'triangular' profile is insufficient to characterize strain rates across a fault.

295 The effect of using degraded data on calculated recurrence intervals is shown for the
296 Parasano-Pescina fault in Figure 6. The different throw profiles modify the implied $\geq M_w 5.1$
297 average earthquake recurrence intervals from 420yrs ('all data') to 465yrs, 262yrs and 524yrs for
298 the 'no max', 'boxcar-max', and 'triangular' throw profile cases respectively.

299 Figure 7 shows site-specific spectral shaking for an example fault can be altered beyond the
300 1σ uncertainty if a simplified fault geometry is assumed that does not include strike-variable
301 geometry. We show the shaking derived from using our measured, detailed fault geometry and
302 two examples of simplified planar fault geometry to demonstrate this point. We use an example
303 site, which has Rjb distance to the Pescasseroli fault of 4.6km when utilizing the detailed fault
304 trace and measurements of dip. However, this distance in increased to 6.4km and 11.3km if the
305 fault is simplified to having planar geometry between the tips with the dip projected from the
306 maximum throw site and tip respectively (see Figure 7a). Figure 7b shows how degrading the
307 fault geometry - so that the fault becomes planar - changes calculated ground shaking from that
308 fault at the specified example site by altering the source-to-site distance (solid line compared to
309 dashed and dotted lines). Figure 7c shows the combined effect of degrading both the fault
310 geometry and throw profiles (dotted and dashed lines). For this fault, the 475yr return period
311 PGA for a given site varies from 0.23g (±1σ: 0.21-0.24g) given the actual fault geometry to
312 0.20g or 0.13g when relying on simplified tip-to-tip planar fault geometries with the dip
313 projected from the maximum throw data site or from the fault tip respectively. If the simplified
314 throw profiles are added to the simplified planar fault geometries for this example fault, this
315 reduces the 475yr PGA to as low as 0.12g (52% of the 'all data' case using detailed geometry)
316 compared to the 0.23g (±1σ: 0.21-0.24g) for the actual fault geometry and detailed throw dataset,
317 a difference that is bigger than the uncertainty on the latter. This is because a fault's non-

318 planarity alters the fault-to-site distance and simplified throw profiles change calculated rates of
319 occurrence. A similar result can be observed in terms of SA(1s) (Figure 7). The observed
320 discrepancies in the observed shaking intensities between simplified and detailed fault geometry
321 further increase at higher mean return periods (lower annual rates of exceedance) (Figure 7c).

322

323 **Discussion**

324 Constraining slip rate has been cited as one of the key uncertainties in earthquake probability
325 calculations (*Field et al., 2014*). For example, in California UCERF3 slip rates are directly
326 constrained for less than half the fault segments (*Field et al., 2014*). Detailed data showing how
327 throw rates and fault geometry vary along a fault are rarely available. Therefore, how these
328 parameters change along the length of a fault generally needs to be inferred from just one or a
329 few measurements. For fault-based PSHA the importance of using such extrapolations needs to
330 be known. In this paper we show that key outputs from fault-based PSHA vary dramatically if
331 the inferred along-strike throw rate (and hence slip rate) profile is in error.

332 For our degraded data sets used for calculating recurrence intervals and ground shaking, we
333 included the data we considered most likely to be present in a less detailed dataset, in other
334 words, the long-term throw data most likely to be collected when only one or a few
335 measurements are taken to represent the throw along the entire fault. We considered the case
336 where only one data site exists along the fault and extrapolated this using 'boxcar-max' and
337 'triangular' throw profiles. In these two scenarios, we assumed that the most likely location
338 where data may be collected would be the site of maximum offset due to it being the most likely
339 site to have identifiable and preserved offset features. In addition, for an example fault we
340 studied the effect of a scenario where detailed data has been collected, but not from the site of

maximum throw: the 'no max' case (ii). In the studied fault, the maximum offset occurs across a bend in the fault, as expected from the geometry-dependent throw rate model in *Faure Walker et al. (2009, 2015)*, so this degraded data scenario represents a case where the bend is not identified, leading to exclusion of a site of higher throw. We show this example to highlight the importance of ensuring data is not excluded along locations with variable geometry. The strain rate calculated using the integrated average throw does lie within the 'all data' case error for nine of the 14 faults, however, for five of the faults an average throw is insufficient. We emphasize that in general fewer measurements than what we have are available for calculating an average throw and hence using average throw rates or slip rates will likely cause worse results than shown. We have not determined a general rule as to whether using average throw rates would more likely overestimate or underestimate the strain rate across a fault because it is dependent on which throw rate measurements are incorporated in the calculation of the average throw rate. We show the 'boxcar-min' and 'boxcar-max' scenarios to demonstrate the range of possible values that could be obtained from using an "average" throw rate when this is calculated from fewer data points. Therefore, we argue that using an "average" throw or slip projected along the fault is also insufficient for modeling hazard.

If the problems with extrapolating data are not recognized, this can lead to large errors in recurrence interval calculations. To put this into perspective we discuss how this compares to the effect of temporal variability in the recurrence intervals due to earthquake clustering. Values of the coefficient of variation (CV, standard deviation of the recurrence interval divided by the mean recurrence interval) generally used in PSHA are <0.5 as this is consistent with values computed (e.g. 0.38 (*Gonzalez et al., 2006*); 0.14-0.34 (*Pace et al., 2006*); 0.48 (*Lienkaemper and Williams, 2007*); 0.2-0.39 (*Visini and Pace, 2014*)). Half our strain rates calculated using the

364 simplified throw rate scenarios lead to values <0.5 or >1.5 times the ‘all data’ case; this
365 demonstrates that using detailed throws changes probability calculations beyond the uncertainty
366 due to intrinsic natural variability.

367 We also demonstrate that if the compounded effect of using simplified planar fault geometry
368 and simplified throw profiles on calculated ground shaking exceedance probabilities is not
369 considered, this will lead to errors in values that inform building code regulations. For the
370 example Pescasseroli fault, the 475yr return period PGA is altered beyond 1σ error and thus our
371 results are significant, for instance, to building code 'ultimate limit state' and ‘life-safety’. The
372 observed differences further increase at higher mean return periods, for instance for the 2475yr
373 PGA or SA(1s), corresponding to collapse prevention in several international building codes and
374 in the IBC08. For other faults, whether ground shaking calculated from simplified throw rates
375 and planar geometries is higher or lower than the ‘all data’ case will depend on both the impact
376 on the recurrence intervals and changes in modeled source-to-site distances. To what extent and
377 to how far from a fault the calculated ground shaking could be impacted by performing
378 calculations based on simplified planar fault geometry and a simplified throw or slip profile is
379 likely to be a function of how variable the actual fault geometry is. Note that local calculations in
380 shaking intensities near faults could be further altered where there are dramatic local variations
381 in fault strike. For instance, along a strongly non-planar fault such as the Fiamignano fault
382 (Figure 3), planar fault models could underestimate local shaking intensities by mislocating a site
383 from the hangingwall onto the footwall. Therefore, the non-planarity of faults, detailed changes
384 in throw rates along faults and local dramatic changes in fault strikes could have significant
385 impact for local planning and disaster management through building regulation impacts. At a
386 regional scale, changes in implied exceedance probabilities of implied shaking (PGA or SA) will

387 have impact on the calculated damage state and hence calculated losses in catastrophe models
388 used within the insurance industry. To achieve high-resolution risk mapping, detailed fault
389 parameters need to be included.

390 We note that a full hazard analysis could use a combination of GMPEs, through a logic-tree
391 approach (e.g. *Bommer et al., 2005*). These should include epistemic uncertainties such as site-
392 specific properties and dip propagation with depth. However, in this paper we use just one set of
393 GMPEs to demonstrate the relevance of geometry. The *Bindi et al. (2011)* GMPEs were chosen
394 because they perform well in the region. Specifically, they performed better than older GMPEs
395 for calculating predicted shaking intensities at stations following the 24th August 2016 Amatrice
396 earthquake (*Meletti et al., 2016*; *D'Ayala et al, 2017*).

397 Most hazard assessments (for earthquakes and other natural hazards) are at a lower spatial
398 resolution than would be desirable for planners (e.g. *Pile et al., 2018*); this is particularly
399 pertinent in areas with critical infrastructure and highly populated areas. Fault-derived hazard
400 maps allow seismic hazard to be calculated at a high spatial resolution (e.g. *Deligiannakis et al.,*
401 *2018*). However, a balance has to be achieved between increasing resolution and any
402 accompanying increases in uncertainty, so understanding how a lack of detailed fault knowledge
403 affects fault-based hazard calculations and associated uncertainties is needed. We have shown
404 herein that calculating exceedance probabilities of shaking intensities at a high spatial resolution
405 requires detailed throw rate and geometry measurements as simplifying these can create results
406 beyond 1σ uncertainty. Therefore, we advocate the use of fault data to increase resolution, but
407 with caution of including appropriate uncertainties where detailed data is lacking. In contrast to
408 fault-based hazard assessments, those based solely on historical shaking or instrumental
409 seismicity data have a restricted resolution because they divide the catalogue of earthquakes

amongst seismic source zones (e.g., *Meletti et al.*, *2008*). These are polygons drawn on maps enclosing large areas with similar historical seismicity. Fault traces are not used, but instead the polygons represent areas that enclose one or more suspected seismic sources. Earthquake probabilities are calculated in each polygon using the rate of historical seismicity (e.g. *Meletti et al.*, *2008*). It is the size of these polygons that limits the spatial resolution of the hazard maps, which in turn is limited by the available historical or seismicity data.

We have not determined herein what spatial resolution of throw rate data is required for resolving the along-strike throw rate profiles of faults with sufficient detail to capture the variations in throw rates such that more measurements do not change inferred recurrence intervals. In terms of resolving individual paleoearthquake magnitudes along a fault from trench sites, *Hintersberger and Decker (2015)* found that 4-6 observation sites were required. We have used at least 4 sites along each fault in our analysis to represent the 'all data' cases for the 14 faults studied, equivalent to measurements with average inter-site spacing of 200m to 6km. The geometry-dependent throw rate model (*Faure Walker et al., 2009; 2015*) suggests that faults with a higher along-strike variation in geometry would likely have a corresponding greater variation in throw rate along the strike. This might suggest that using simplified throw rate profiles is sufficient if faults are relatively planar (e.g. *D'Amato et al., 2017*), but not if the fault has more variable fault geometry. This has not been tested, but intuitively it is clear that more sites are needed for faults with greater non-planarity. To determine the required spatial resolution, we need a greater number of examples of faults with multiple data sites.

Currently such detailed geometry and throw rate data with multiple data points on each fault is not available and in some areas it may be difficult to obtain it by ground-based field methods. However, we note that techniques to capture such data - such as TLS (terrestrial laser scanning),

433 ALS (airborne LiDAR scanning) and structure from motion photogrammetry - are making the
434 data acquisition increasingly possible (e.g. see *Telling et al. (2017)* for a review of improvements
435 in modeling fault geometries with TLS). With increasing capabilities to measure such detail we
436 argue that as such data become available they should be used. In addition, throw rates can be
437 constrained from paleoseismic trench studies. However, such studies need to use multiple sites
438 along a fault and consider fault geometry when extrapolating point data along a fault or input
439 into calculations like those in *Faure Walker et al. (2009)* so that along strike variations in throw
440 rate can be calculated relative to constrained sites.

441 In addition to including detailed geometry for calculating earthquake rates and ground
442 shaking intensities, we suggest that it should also be used for other aspects of hazard
443 calculations. For example, the effect of Coulomb stress transfer is sometimes included in
444 earthquake probability calculations (e.g. *Pace et al., 2014*). We note that there are increasing
445 capabilities to input fault geometry detail in Coulomb stress transfer calculations, with existing
446 studies demonstrating the need for strike-variable geometry (*Mildon et al. 2016b; 2017*).

447 Overall, we argue that fault slip rates are needed to inform seismic hazard calculations rather
448 than relying on historical records alone, however we have demonstrated herein the importance of
449 using detailed along-fault throw rate profiles and detailed fault geometry for these. Without such
450 data, hazard calculations used to inform government, industry, and residents may misinform
451 about the geography of seismic hazard and hence not trigger appropriate action to mitigate
452 against future events. Our results highlight that local 3D fault geometry and local throw rates
453 must be considered when extrapolating data from individual sites along a fault for use in fault-
454 based PSHA. We have demonstrated the importance of detailed data for calculating strain rates
455 and hence earthquake moment release across faults (*Faure Walker et al., 2009; 2010; Wilkinson*

456 *et al., 2015*), earthquake recurrence intervals averaged over multiple earthquake cycles, and
457 expected shaking calculated using GMPEs. For individual towns, multiple faults will affect the
458 probabilities of different shaking intensities so the changes for the individual faults shown here
459 will be compounded. Therefore, we are advocating a change in how fault slip rates and geometry
460 are considered in PSHA calculations.

461

462 **Conclusions**

463 We find that using detailed fault throw profiles and fault geometries that vary along strike
464 can have significant impact on calculated hazard calculations by altering recurrence rates and
465 ground shaking intensities at specific sites respectively. We show that probability calculations
466 change beyond the uncertainty due to intrinsic natural variability and site-specific shaking
467 intensities change beyond the uncertainty bounds of GMPEs. Therefore, we argue that either
468 detailed data should be used when calculating hazard or that such variations should be
469 considered within uncertainties of fault-based PSHA.

470 We studied 14 active normal faults within the central Apennines for which we have four or
471 more sites constraining the post 15ka throw rate. Calculating strain rates across these faults from
472 simplified 'boxcar-max', 'boxcar-mean', 'boxcar-min' and 'triangular' throw profiles resulted in
473 only one, nine, two and three of the faults having strain rates lie within 1 sigma error of the 'all
474 data' case respectively. For the simplified cases, calculated strain rates vary from 51% to 303%
475 relative to the 'all data' cases with half of them having calculated strain rates <0.5 or >1.5 times
476 the 'all data' cases. These results demonstrate how far from the actual rates simplifications can
477 cause the strain rates to be.

For an example fault, the Parasano-Pescina fault, using simplified throw rate profiles modifies the implied $\geq M_w 5.1$ average earthquake recurrence intervals from 420yrs ('all data') to 465yrs, 262yrs and 524yrs for the 'no max', 'boxcar-max', and 'triangular' throw profile cases respectively.

For another example fault, the Pescasseroli fault, the 475yr return period PGA for a given site a few kilometers (R_{jb} 4.6km) from the fault varies from 0.41g ($\pm 1\sigma$: 0.37-0.44g) given the actual fault geometry and throw-profile to 0.34g or 0.24g when relying on simplified tip-to-tip planar fault geometries with the dip projected from the maximum throw site or from the fault tip respectively. Using simplified throw profiles and planar fault geometries for this example fault alters the 475yr PGA to as low as 0.19g (46% of the 'all data' case using detailed geometry).

Data and Resources

The data used in this paper came from published sources listed in the references and new data in Table 1. Figure 3 was made using the Generic Mapping Tools version 5.2.1 (www.soest.hawaii.edu/gmt; Wessel and Smith, 1998).

Acknowledgements

Some of the fieldwork in this study was funded by NERC Grant NE/I024127/1 and NERC Studentship award NE/L501700/1. Our manuscript was improved through anonymous review and editor comments.

499 **References**

500

501 Allen J., Brandte U., Brauer A., Hubbertens H.-W., Huntley B., Keller J., Kraml M., Mackensen
502 A., Mingram J., Negendank J., et al., 1999, Rapid environmental changes in southern Europe
503 during the last glacial period, Nature, 400, 740–743

504

505 D'Amato D., Pace B., Di Nicola L., Stuart F.M., Visini F., Azzaro R., Branca S., Barford D.N.
506 (2017) Holocene slip rate variability along the Pernicana fault system (Mt. Etna, Italy): Evidence
507 from offset lava flows, GSA Bulletin 129 (3-4) 304-317

508

509 Assatorians K. and Atkinson G.M. (2013) EqHaz: An Open-Source probabilistic seismic-hazard
510 code based on the Monte Carlo simulation approach, *Seismological Research Letters,* 84 (3),
511 516-524, DOI 10.1785/0220120102

512

513 Bindi D., Pacor F., Luzi L., Puglia R., Massa M., Ameri G., Paolucci R., (2011), Ground Motion
514 Prediction Equations derived from the Italian strong motion database, Bulletin of Earthquake
515 Engineering, 9 (6) 1899-1920

516

517 Bird P. and Kagan Y.Y., (2004), Plate-Tectonic Analysis of Shallow Seismicity: Apparent
518 Boundary Width, Beta, Corner Magnitude, coupled Lithosphere Thickness, and Coupling in
519 Seven Tectonic Settings, Bulletin of the Seismological Society of America, 94 (6), 2380-2399

Blumetti A.M., Grutzner C., Guerrieri L. and Livio F., (2017), Quaternary earthquakes: Geology and palaeoseismology for seismic hazard assessment, Quaternary International, 451, 1-10

Bommer J.J. and Akkar S., (2012) Consistent Source-to-Site Distance Metrics in Ground-Motion Prediction Equations and Seismic Source Models for PSHA, *EARTHQUAKE SPECTRA*, 28, 1-15, ISSN: 8755-2930

Bommer J.J., Scherbaum F., Bungum H., Cotton F., Sabetta F., Abrahamson N.A. (2005), On the use of Logic Trees for Ground Motion Prediction Equations in seismic hazard analysis, *Bulletin of the Seismological Society of America,* 95 (2) 377-389, DOI:10.1785/0120040073

Camelbeeck, T., Vanneste, K., Alexandre, P., Verbeeck, K., Petermans, T., Rosset, P., Everaerts, Warnant, R., and van Camp, M., (2007) Relevance of active faulting and seismicity studies to assessments of long-term earthquake activity and maximum 20 magnitude in intraplate northwest Europe, between the Lower Rhine Embayment and the North Sea. Geol. Soc. Am. Spec. Pap. 425, 193-224

Cartwright J.A. and Mansfield C.S., (1998), Lateral displacement variation and lateral tip geometry of normal faults in the Canyonlands National Park, Utah, *Journal of Structural Geology*, 20 (1) 3-19

Cheloni D., De Novellis V., Albano M., Antonioli A., Anzidei M., Atzori S., Avallone A., Bignami C., Bonano M., Calcaterra S., et al., (2017) Geodetic model of the 2016 Central Italy earthquake sequence inferred from InSAR and GPS data, *Geophysical Research Letters,* 44, 6778–6787, doi:10.1002/2017GL073580.

Civico R, Pucci S, Villani F, Pizzimenti L, De Martini PM, Nappi R, and the Open EMERGEO Working Group (2018) Surface ruptures following the 30 October 2016 Mw6.5 Norcia earthquake, central Apennines, *Journal of Maps,* 151-160 DOI: 10.1080/17445647.2018.1441756

Contreras J., Anders M.H., and Scholz C.H. (2000) Growth of a normal fault system: observations from the Lake Malawi basin of the east African rift, *Journal of Structural Geology*, 22, 159-168

Cowie P., Scholz C., Roberts G., Faure Walker J.P., Sheer P. (2013) Viscous roots of active seismogenic faults revealed by geologic slip rate variations, *Nature Geoscience*, 6, 1036-1040

Cowie PA, Phillips RJ, Roberts GP, McCaffrey K, Zijerveld LJJ, Gregory LC, Faure Walker JP, Wedmore LNJ, Dunai TJ, Binnie SA, et al., (2017) Orogen-scale uplift in the central Italian Apennines drives episodic behaviour of earthquake faults, *Scientific Reports,* 7, doi:10.1038/srep44858

D'Ayala D, Alexander D, De Luca F, Del Gobbo G, Galasso C, Lloyd T, Mildon Z, Morgan E, Pedicone D, Perugini P, Putrino V, Totaro A, Tagliacozzo S, Faure Walker J, (2017). Earthquake Engineering Field Investigation Team (UK) – Data and Discussion on the 2016 Central Italy Mission, *16th World Conference on Earthquake Engineering (16WCEE), Santiago, Chile*

Deligiannakis G., Papanikolaou I.D., Roberts G., 2018, Fault specific GIS based seismic hazard maps for the Attica region, Greece, *Geomorphology*, 306 264-282, ISSN 0169-555X

Faure Walker, J.P., Roberts, G.P., Cowie, P.A., Papanikolaou, I., Michetti, A.M., Sammonds, P., Phillips, R., (2009). Horizontal strain rates and throw rates across breached relay-zones, central Italy: implications for the preservation of throw deficits at points of normal fault linkage, *Journal of Structural Geology* 31 1145-1160 doi:10.1016/j.jsg.2009.06.011

Faure Walker, J.P. (2010) Mechanics of Continental Extension in the Italian Apennines, *PhD Thesis, University College London*

Faure Walker, J.P., Roberts, G.P., Sammonds, P., Cowie, P.A.C., (2010). Comparison of earthquake strains over 100 and 10,000 year timescales: insights into variability in the seismic cycle in the central Apennines, Italy. Journal of Geophysical Research 115 (B10418) doi:10.1029/2009JB006462.

584

585 Faure Walker, J.P., Roberts, G.P., Cowie, P.A., Papanikolaou, I., Michetti, A.M., Sammonds, P.,
586 Wilkinson M., McCaffrey K. & Phillips R. (2012) Relationship between topography, rates of
587 extension and mantle dynamics in the actively-extending Italian Apennines, *Earth and Planetary*
588 *Science Letters* 325-326, 76-84

589

590 Faure Walker, J.P., Roberts, G.P., Cowie, P.A., McCaffrey K., Wedmore L., Watson Z., Gregory
591 L., (2015) Long-term strain rates as a tool for understanding the mechanics of continental
592 extension and the importance of local 3D fault geometry for local throw rates across faults. *6th*
593 *Int. INQUA Meeting on Paleoseismology, Active Tectonics and Archaeoseismology, 19-24 April*
594 *2015*, Pescina, Fucino Basin, Italy, *Miscellanea INGV ISSN 2039-6651 2015_Numero* 27 150-
595 154

596

597 Field G. P. Biasi G.P., Bird P., Dawson T.E., Felzer K.R., Jackson D.D., Johnson K.M., Jordan
598 T.H., Madden C. Michael A.J., et al., (2014). Uniform California Earthquake Rupture Forecast,
599 Version 3 (UCERF3) - The time-independent model, *Bulletin of the Seismological Society of*
600 *America* 104 (3) 1122–1180, doi:10.1785/0120130164

601

602 Galadini, F. and Galli, P., (2003) Paleoseismology of silent faults in the Central Apennines
603 (Italy): the Mt. Vettore and Laga Mts. faults, *Annals of Geophysics*, 46(5), 815–836.

604

605 Galli, P., F. Galadini, and D. Pantosti (2008), Twenty years of paleoseismology in Italy, *Earth*

606 *Science Reviews*, 88, 89–117.

607

608 Giraudi C. and Frezzotti M., Inversione pleistocenica del drenaggio in alta Val Roveto (Abruzzo
609 sud occidentale) (1986), *Mem. Soc. Geol. It.,* 35, 847-853

610

611 Giraudi G. and Frezzotti M., (1997) Late Pleistocene Glacial Events in the Central Apennines,
612 Italy, *Quaternary Research*, 48, 280-290

613

614 Gonzalez, A., J. B. Gomez, and A. F. Pacheco (2006). Updating seismic hazard at Parkfield,
615 *Journal of Seismology* 10 (2) 131–135

616

617 Hintersberger E. and Decker K. (2015), Estimating magnitudes of paleo-earthquakes from
618 multiple observations, *6th Int. INQUA Meeting on Paleoseismology, Active Tectonics and*
619 *Archaeoseismology, 19-24 April 2015*, Pescina, Fucino Basin, , Italy, *Miscellanea INGV ISSN*
620 *2039-6651 2015_Numero* 27 207-208

621

622 Hintersberger E., Decker K., Lomax J., Luthgens C. (2018) Implications from
623 palaeoseismological investigations at the Markgrafneusiedl Fault (Vienna Basin, Austria) for
624 seismic hazard assessment, *Natural Hazards and Earth Systems,* 18, 531-553, doi:
625 10.5194/nhess-18-531-2018

626

627 Iervolino I., Galasso C., Paolucci R., Pacor F. (2011) Engineering ground motion record
628 selection in the Italian Accelerometric Archive. *Bulletin of Earthquake Engineering*, 9(6):1761-
629 1778.

630

631 Iezzi F., Mildon Z., Faure Walker J.P., Roberts G., Goodall H., Wilkinson M., Robertson J.,
632 Coseismic throw variation across along-strike bends on active normal faults: implications for
633 displacement/length scaling of seismic rupture, *submitted manuscript*

634

635 Jackson D.D. and Kagan Y.Y., (2006) The 2004 Parkfield earthquake, the 1985 prediction, and
636 characteristic earthquakes: Lessons for the future, *Bulletin of the Seismological Society of*
637 *America* 96 (4B), S397-S409

638

639 Kagan Y.Y. (2002) Seismic moment distribution revisited: I. Statistical results, *Geophysical*
640 *Journal International* 148 520-541

641

642 Kostrov V.V., (1974) Seismic Moment and Energy of Earthquakes, and Seismic Flow of Rock,
643 Izv., Earth Physics,1, 23-40 (translation UDC 550.341, 13-21)

644

645 Lienkaemper, J. J., and P. L. Williams (2007). A record of large earthquakes on the southern
646 Hayward fault for the past 1800 years, *Bulletin of the Seismological Society of America* 97 (6)
647 1803–1819, doi: 10.1785/0120060258.

Liu M., Stein S., and Wang H., (2011), '2000 years of migrating earthquakes in North China: How earthquakes in midcontinents differ from those at plate boundaries' *Lithosphere*, vol 3, no. 2, pp. 128-132. DOI: 10.1130/L129.1

Liu M. and Stein S., (2016) Mid-continental earthquakes: Spatiotemporal occurrences, causes, and hazards *Earth-Science Reviews*, 162, 364-386

Livio F., A.M. Michetti, E. Vittori, L. Gregory, L. Wedmore, L. Piccardi, E. Tondi, G. Roberts, A.M. Blumetti, L. Bonadeo, F. et al., Surface faulting during the August 24, 2016, Central Italy earthquake (Mw 6.0): preliminary results, (2016) *Annals of Geophysics*, 59 (5), DOI: 10.4401/ag-7197

Manighetti, I., M. Campillo, C. Sammis, P.M. Mai and G. King, (2005). Evidence of self-similar, triangular slip distributions on earthquakes: Implications for earthquakes and fault mechanics. *Journal of Geophysical Research*. 110, B05302.

McClymont A.F., Villamor P. and Green A.G. (2009) Fault displacement accumulation and slip rate variability within the Taupo Rift (New Zealand) based on trench and 3-D ground-penetrating radar data, *Tectonics* 28 (4), DOI: 10.1029/2008TC002334

669 Meletti C., Galadini F., Valensise G., Stucchi M., Basili R., Barba S., Boschi E., (2008) A
670 seismic source zone model for the seismic hazard assessment of the Italian territory,
671 *Tectonophysics*, 450, 1-4, 85-108

672

673 Meletti C., Visini F., D'Amico V., Rovida A. (2016), Seismic Hazard in Central Italy and the
674 2016 Amatrice earthquake, Annals of Geophysics, 59 DOI: 10.4401/AG-7248

675

676 Mildon Z.K., Roberts G., Faure Walker J.P., Iezzi F. (2017), Coulomb stress transfer and fault
677 interaction over millennia on non-planar active normal faults: the Mw 6.5-5.0 seismic sequence
678 of 2016-2017, central Italy, *Geophysical Journal International* 210 (2) 1206-1218

679

680 Mildon Z.K., Roberts G., Faure Walker J.P., Wedmore L., McCaffrey K. (2016a) Active normal
681 faulting during the 1997 seismic sequence in Colfiorito, Umbria: Did slip propagate to the
682 surface? *Journal of Structural Geology* 91 102-113

683

684 Mildon Z.K., Toda S., Faure Walker J.P., Roberts G. (2016b), Evaluating models of Coulomb
685 stress transfer - is variable fault geometry important? *Geophysical Research Letters* 43

686

687 Mildon Z. K., (2017) The link between earthquakes and structural geology; the role of elapsed
688 time, 3D geometry and stress transfer in the central Apennines, Italy. *Doctoral thesis, UCL*
689 *(University College London)*

690

691 Morewood N.C. and Roberts G.P., (2000) The geometry, kinematics and rates of deformation
692 within an en echelon normal fault boundary, central Italy, Journal of Structural Geology, 22,
693 1027-1047

694

695 Pace, B., L. Peruzza, G. Lavecchia, and P. Boncio (2006). Layered seismogenic source model
696 and probabilistic seismic-hazard analyses in central Italy, *Bull. Seism. Soc. Am.* 96 (1) 107 –132

697

698 Pace, B., Bocchini G.M., Boncio P., (2014) Do static stress changes of a moderate-magnitude
699 earthquake significantly modify the regional seismic hazard? Hints from the L'Aquila 2009
700 normal-faulting earthquake (Mw 6.3, central Italy), *Terra Nova*, 26 430-439, DOI:
701 10.1111/ter.12117

702

703 Pace B., Visini F., Peruzza L., (2016) *FiSH*: MATLAB Tools to Turn Fault Data into Seismic
704 Hazard Models, *Seismological Research Letters*, DOI: 10.1785/0220150189

705

706 Palumbo, L., Benedetti L., Bourles D., Cinque A., and Finkel R., (2004), Slip history of the
707 Magnola fault (Apennines, central Italy) from 36Cl surface exposure dating: evidence for strong
708 earthquakes over the Holocene, *Earth and Planetary Science Letters*, 225, 163–176.

709

710 Papanikolaou I.D., Roberts G.P., and Michetti A.M., (2005) Fault scarps and deformation rates

711 in Lazio-Abruzzo, Central Italy: Comparison between geological fault slip rate and GPS data,
712 Tectonophysics, 408, 147-176, 2005

713

714 Papanikolaou I.D. and Roberts G.P., (2007) Geometry, kinematics and deformation rates along
715 the active normal fault system in the southern Apennines: Implications for fault growth, Journal
716 of Structural Geology, 29, 166-188, 2007

717

718 Papanikolaou I.D., Van Balen R., Silva P.G., Reicherter K. (2015) Geomorphology of active
719 faulting and seismic hazard assessment: New tools and future challenges, Geomorphology 237 1-
720 13

721

722 Piccardi L., Gaudemer Y., Tapponier P., and Boccaletti M., (1999) Active oblique extension in
723 the central Apennines (Italy): evidence from the Fucino region, Geophysical Journal
724 International, 139, 499-530

725

726 Pile J., Gouramanis C., Switzer A.D., Rush B., Reynolds I., Soria J.L.A. (2018) Can the risk of
727 coastal hazards be better communicated? *International Journal of Disaster Risk Reduction*, 27,
728 439-450

729

730 Pucci, S., De Martini P.M., Civico R., Villani F., Nappi R., Ricci T., Azzaro R., Brunori C.A.,
731 Caciagli M., Cinti F.R. et al. (2017), Coseismic ruptures of the 24 August 2016, M_w 6.0 Amatrice

732 earthquake (central Italy), Geophys. Res. Lett., 44, 2138–2147, doi:10.1002/2016GL071859.

733

734 Reilly C., Nicol A. and Walsh J., (2016) Importance of pre-existing fault size for the evolution of
735 an inverted fault system, *Geological Society, London, Special Publications,* 439, 447-463 DOI:
736 10.1144/SP439.2

737

738 Roberts, G.P., Michetti, A.M., (2004) Spatial and temporal variations in growth rates along
739 active normal fault systems: an example from the Lazio-Abruzzo Apennines, central Italy. *J.*
740 *Struct. Geol.* 26, 339–376.

741

742 Roberts, G. P. (2007), Fault orientation variations along the strike of active normal fault systems
743 in Italy and Greece: Implications for predicting the orientations of subseismic-resolution faults in
744 hydrocarbon reservoirs, *AAPG Bull.* 91(1), 1–20.

745

746 Roberts, G. P. (2007), Fault orientation variations along the strike of active normal fault systems
747 in Italy and Greece: Implications for predicting the orientations of subseismic-resolution faults in
748 hydrocarbon reservoirs, *AAPG Bull.* 91(1), 1–20.

749

750 Rosetto, T., Gehl, P., Minas, S., Galasso, G., Duffour P., Douglas, J., and Cook, O., (2016)
751 FRACAS: A capacity spectrum approach for seismic fragility assessment including record-to-
752 record variability, *Engineering Structures*, 125 337-348, doi: 10.1016/j.engstruct.2016.06.043

Stein, S., R. Geller, and M. Liu (2012), Why earthquake hazard maps often fail and what to do about it, *Tectonophysics*, 562–563, 1–25.

Stucchi M., Meletti C., Montaldo V., Crowley H., Calvi G.M., Boschi E., (2011) Seismic Hazard Assessment (2003-2009) for the Italian Building Code, *Bulletin of the Seimsmological Society of America*, DOI: 10.1785/0120100130

Telling J., Lyda A., Hartzell P., Glennie C., (2017) Review of Earth science research using terrestrial lasar scanning, *Earth Science Reviews*, 169 35-68

Valentini, A., Visini, F., and Pace, B.: (2017) Integrating faults and past earthquakes into a probabilistic seismic hazard model for peninsular Italy, *Natural Hazards and Earth Science Systems*, 17 (11), doi: 10.5194/nhess-17-2017-2017

Villani F, Civico R, Pucci S, Pizzimenti L, Nappi R, De Martini PM, and the Open ERERGEO Working Group (2018), A database of the coseismic effects following the 30 October 2016 Norcia earthquake in Central Italy, *Scientific Data*, 5, doi:10.1038/sdata.2018.49

Visini, F., and Pace, B. (2014) Insights on a key parameter of earthquake forecasting, the coefficient of variation of the recurrence time, using a simple earthquake simulator, *Seismological Research Letters*, 85 (3) 703–713, doi:10.1785/0220130165.

775

776 Wedmore W., Faure Walker J.P., Roberts G., Sammonds P., McCaffrey K., Cowie C. (2017) A
777 667 year record of coseismic and interseismic Coulomb stress changes in central Italy reveals the
778 role of fault interaction in controlling irregular earthquake recurrence intervals, *Journal of*
779 *Geophysical Research*, 122 (7) 5691-5711

780

781 Wedmore, LNJ; (2017) Fault interaction processes and continental extension in the central
782 Apennines, Italy. *Doctoral thesis, UCL (University College London)*

783

784 Wells D.L. and Coppersmith K.J. (1994) New empirical relationships among magnitude, rupture
785 length, rupture width, rupture area and surface displacement, *Bulletin Seismological Society of*
786 *America* 84 974-1002

787

788 Wessel, P., W. H. F. Smith, R. Scharroo, J. F. Luis, and F. Wobbe, (2013) Generic Mapping
789 Tools: Improved version released, *EOS Trans. AGU*, 94, 409-410

790

791 Wilkinson, M., Roberts, G.P. , McCaffrey, K.J.W., Cowie, P.A., Faure Walker, J.P.,
792 Papanikolaou, I.D., Phillips, R.J., Michetti, A.M., Vittori, E. , Gregory, L., et al., (2015) Slip
793 distributions on active normal faults measured from LiDAR and field mapping of geomorphic
794 offsets: an example from L'Aquila, Italy, and implications for modelling seismic moment release,
795 *Geomorphology* 237 130-141

796

797 **Full Mailing List of Each Author (alphabetically)**

798

799 Joanna Faure Walker – Institute for Risk & Disaster Reduction, University College London,
800 Gower Street, London, WC1E 6BT

801 Carmine Galasso – Department of Civil, Environmental & Geomatic Engineering, University
802 College London, London, Gower Street,WC1E 6BT, UK

803 Ken McCaffrey - Department of Earth Sciences, Durham University, Science Labs, Durham
804 DH1 3LE UK

805 Zoe Mildon –Centre for Research in Earth Sciences, University of Plymouth, Drake Circus,
806 Plymouth, Devon, PL4 8AA

807 Gerald Roberts – Department of Earth and Planetary Sciences, Birkbeck College, Malet Street,
808 London, WC1E 7HX, UK

809 Francesco Visini - Istituto Nazionale di Geofisica e Vulcanologia, Via della Faggiola, 32, 56126
810 – Pisa, Italy

811

812 **Tables**

813 Table 1: Fieldwork data used within calculations that have not been previously published.

Fault	UTM X	UTM Y	Slip vector azimuth (°)	Slip vector plunge (°)	15ka throw (m)

Barisciano	369075	4698111	194	51	7.0
	383475	4689190			6.5
	392297	4679321	226	44	6.5
Fucino	393474	4644538	229	52	
	393493	4644535	233	58	
	393541	4644520	209	56	
	393583	4644506	210	58	
	393594	4644503	219	59	
	393636	4644489	220	50	
	393736	4644447	218	40	
Liri	364529	4648418	168	65	
	364554	4648395	173	61	
	364628	4648319	178	67	9
	364633	4648332	189	71	
	364671	4648294	197	64	
	364683	4648271	189	66	
	364722	4648213	177	58	
Ocre	367652	4682645	197	66	

	367884	4682479			6.4
	368647	4681804	211	58	
	368775	4681715	213	46	
	368838	4681676	217	56	
	368939	4681589			2.8
	369008	4681532	260	62	
	369048	4681494	255	55	6.3 ±3.0 *(eye estimate)*
	369068	4681487			4.0
	369251	4681334	217	54	
Roccapreturo	392123	4672914	185	62	
	393537	4671944	237	47	
	393541	4671945			6.5
	393554	4671926	231	50	
	393665	4671836	225	57	
	393699	4671804	215	55	
	393781	4671481	215	59	
	393785	4671635	211	44	
	393791	4671445	213	56	

	393799	4671404	212	53	
	393971	4671229			8.47
	393995	4671211	258	45	
	394004	4671182	258	55	
	395036	4670693	253	52	
Scanno	406678	4642989	209	41	
	406796	4643001			4.5
	406929	4642938	217	47	10.6
	407154	4642786			12.6
	407413	4642561	224	58	
	407452	4642544	217	52	12.3
	407462	4642521	228	54	
	407571	4642414	212	52	
	410765	4637903			4.0

814

815 **Figure captions**

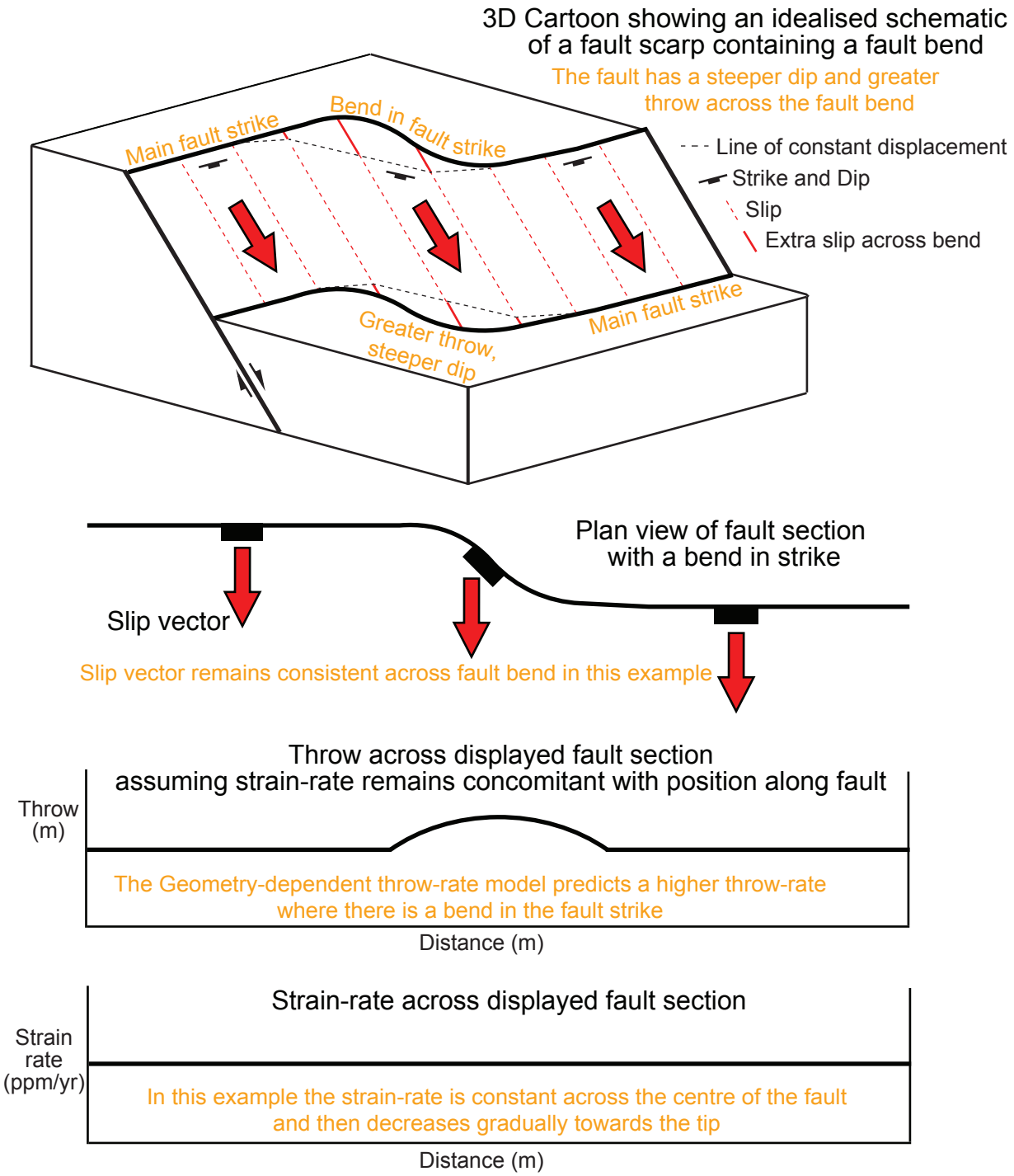

Figure 1: Geometry-dependent throw rate model. The figure shows how, for a given strain rate profile, the throw rate across the fault changes with a change in strike along the fault. In order to keep the strain rate concomitant with its position along a fault, the throw rate varies where there are changes in fault strike and dip. How the strain rate changes along the fault is shown

here for one idealized example. The figure has been adapted from Faure Walker et al. (2015).

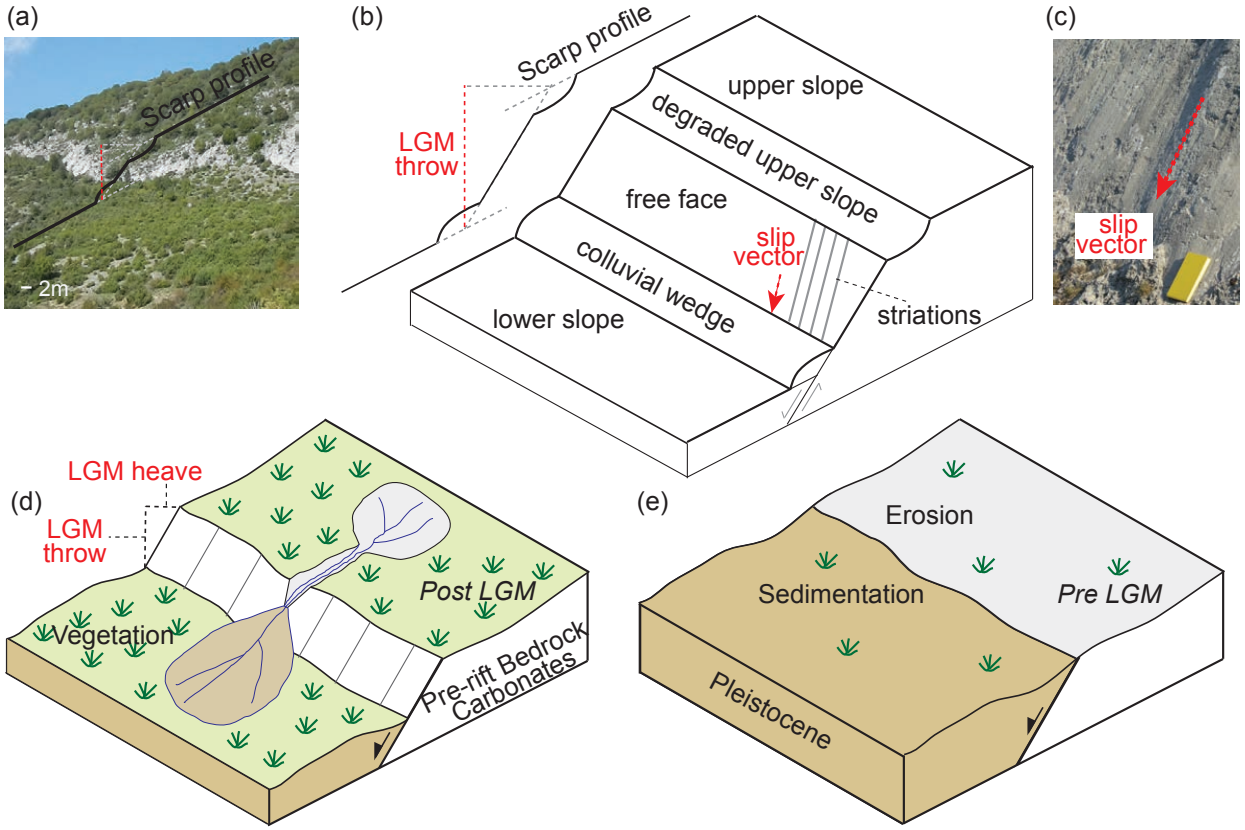

Figure 2: Fault scarps exposed at the surface in the central Italian Apennines formed since the end of the LGM (Last Glacial Maximum). (a) Photograph of a post glacial scarp with example of a scarp profile line. (b) Cartoon topographic scarp profile constructed across cartoon fault scarp showing how the throw since the LGM is constructed. (c) Striations on limestone fault plane revealing slip vector (d) Cartoon showing formation of surface scarp following the LGM, the scarp is exposed because fault slip rates are faster than erosion and sedimentation rates; the LGM provides a time marker since the scarps were formed because during the glacial maximum, as shown in (e), scarps were generally not exposed as erosion and sedimentation rates outstripped fault slip rates. (b) adapted from Faure Walker et al. (2009), (d) and (e) adapted from Roberts and Michetti (2004) and Faure Walker (2010).

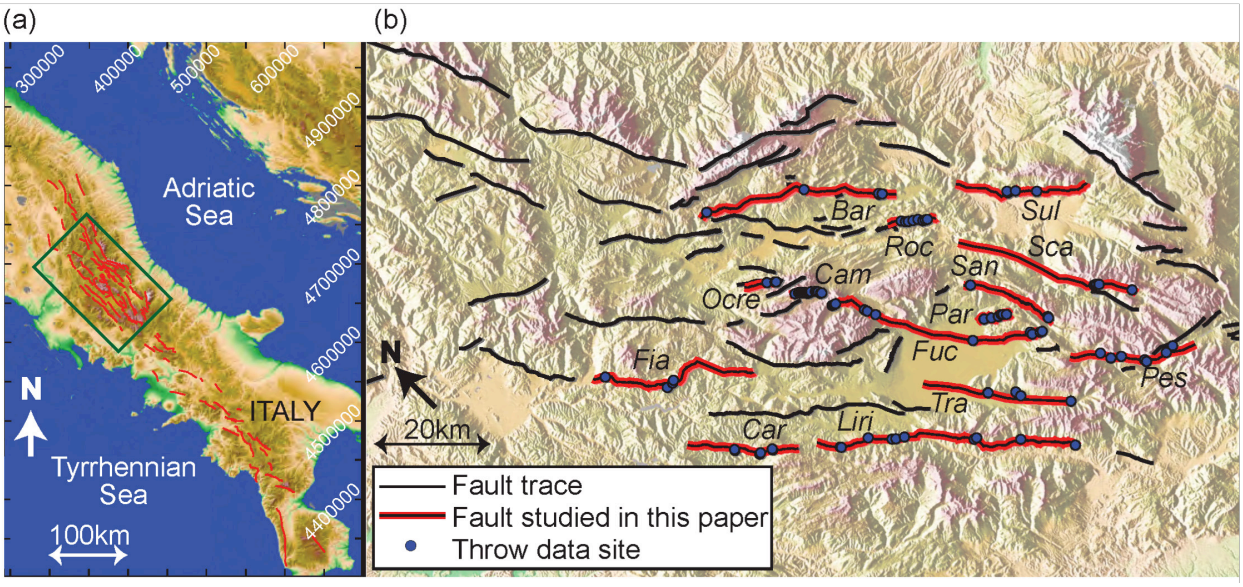

833

834 *Figure 3: Map of the active faults in the central Apennines study region showing studied faults.*
835 *The box in location map (a) shows the area covered by the more detailed map (b) of the 14 faults*
836 *investigated in this study. Along the 14 faults, which are highlighted in red, sites with 15ka throw*
837 *rate measurements are shown with filled in circles. Bar=Barisciano, Cam=Campo Felice,*
838 *Car=Carsoli, Fia=Fiamignano, Fuc=Fucino, Par=Parasano, Pes=Pescasseroli,*
839 *Roc=Roccapreturo, San=San Sebastiano, Sca=Scanno, Sul=Sulmona, Tra=Trasacco. Liri and*
840 *Ocre also marked. Figures produced using GMT (Wessel et al., 2013).*

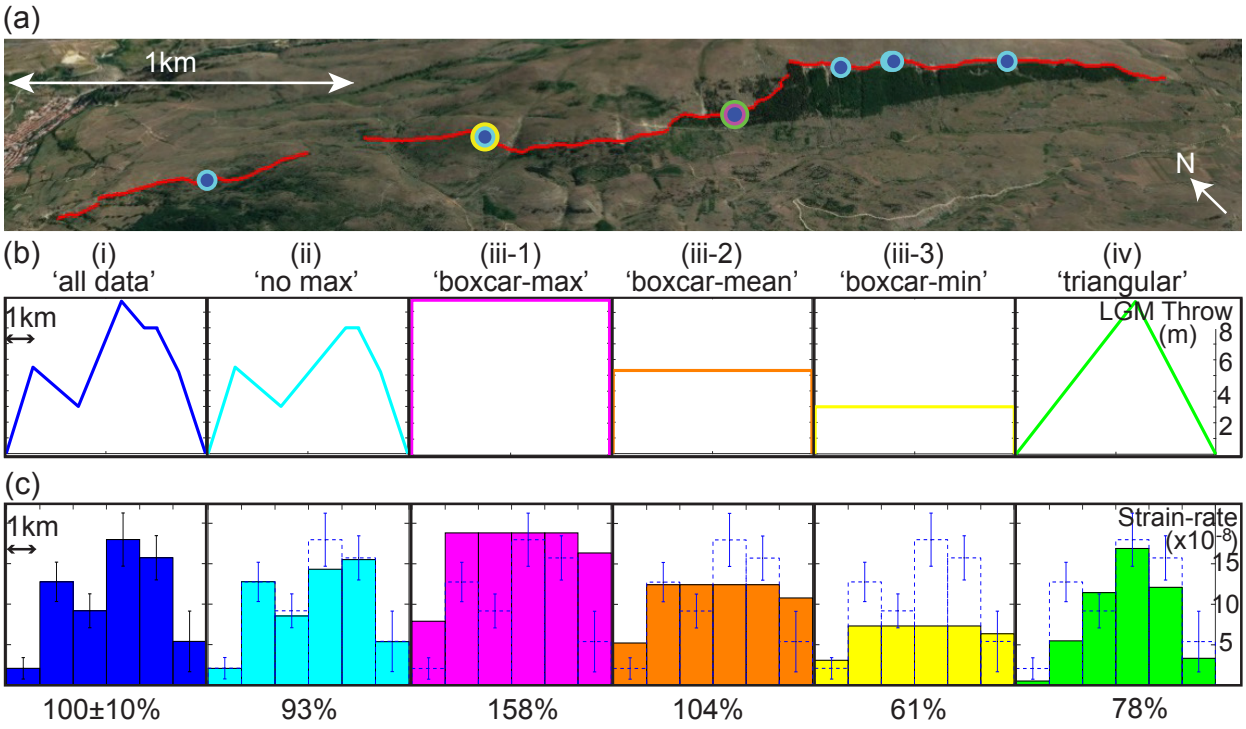

Figure 4: Plots show how 15kyr strain rates in a regular 1x2km grid change along the Parasano-Pescina fault and how using degraded data for the throw profiles affects the calculated strain rates across the fault. (a) Trace of Parasano-Pescina Fault from GoogleEarth™. Circles show sites of post-glacial throw measurements, the colours correspond to which models (i-iv) the throw measurements were used in. (b) Throw profiles along the fault for each of the models and (c) strain rates within 1km x 2km grid boxes along the fault. (i) 'all data' uses all the data from the seven data collection sites along the fault. (ii) 'no max' uses all the data except from the throw rate data collected from the site of maximum 15ka throw. (iii-1) 'boxcar-max' only uses the data from the maximum throw rate site, (iii-2) 'boxcar-mean' uses the average 15ka throw, slip vector azimuth and plunge, and (iii-3) 'boxcar-min' uses only data collected from the minimum throw rate site (above zero). In each 'boxcar' scenario, the value of throw is projected along the entire length of the fault until near the fault tips where the throw rapidly decreases to zero. (iv) 'triangular', like 'boxcar-max' only uses the data from the

maximum throw rate site, but in this scenario the throw rate decreases linearly from the maximum to zero at each tip forming a triangular throw rate profile along the fault. Error bars and dotted bar plots shown in each plot are for the 'all data' case (i). Percentage values in the boxes give the total strain rate across the fault relative to the 'all data' case (i). This shows that degrading data by excluding a single data point (ii) or extrapolating a single throw value along a fault (iii, iv) changes calculated strain rates across the fault.

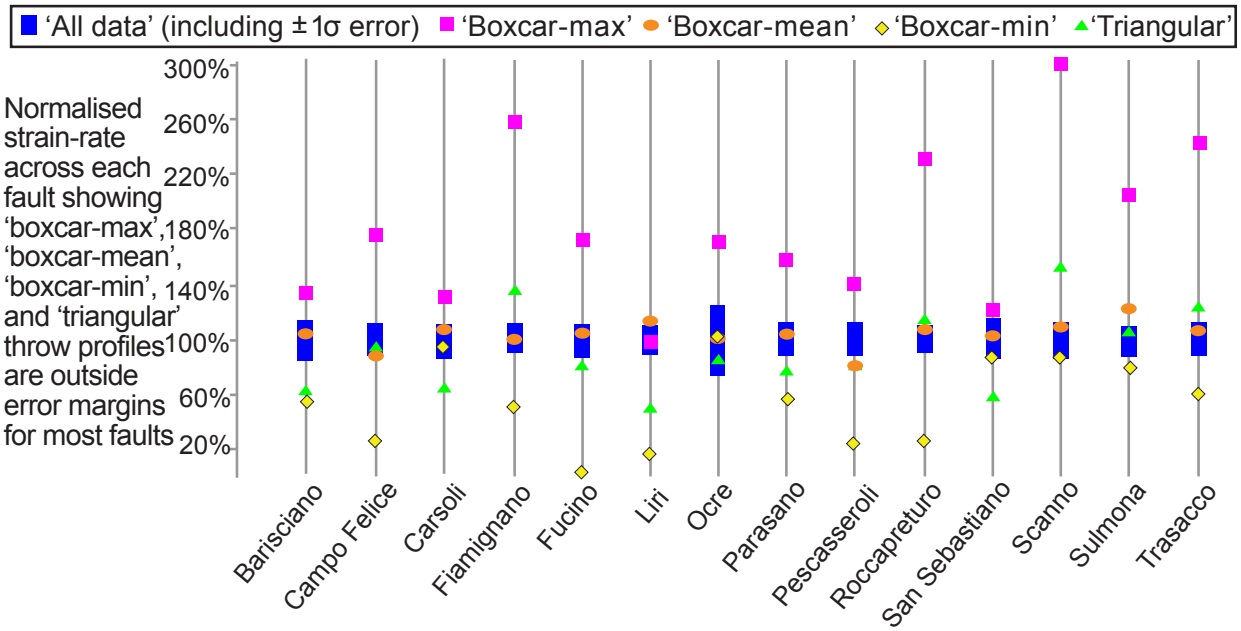

Figure 5: Strain rates calculated across 14 faults using different throw rate profiles: 'all data' case (blue rectangles including ±1σ), 'boxcar-max' (pink squares), 'boxcar-mean' (orange ovals), 'boxcar-min' (yellow diamonds) and 'triangular' (green triangles). The strain rates calculated using simplified throw rate profiles are shown relative to those calculated using the 'all data' throw rate profiles. The inferred strain rates calculated using simplified throw rate profiles mostly lie outside ±1σ uncertainty of the 'all data' strain rates, demonstrating that the simplified throw rate profiles are insufficient for calculating strain rates across faults.

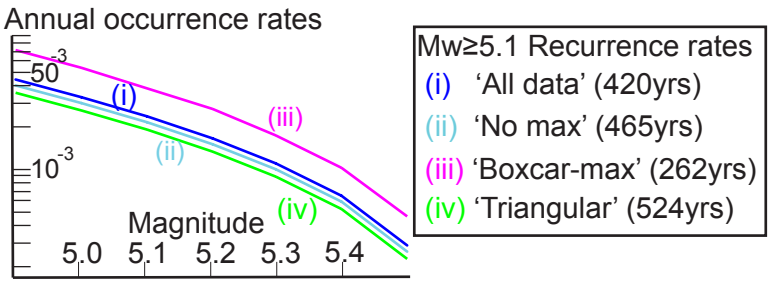

869

870 *Figure 6: Frequency-magnitude semi-log plots for M_w 4.9-5.5 for the four throw-profile*
871 *scenarios along the Parasano-Pescina fault. The graphs compare the (i) all data sites included*
872 *in the 'all data' throw profile with three sets of degraded data. The three sets of degraded data*
873 *are created by: (ii) leaving out the maximum throw point in the 'no max' profile but including*
874 *the other measurements; (iii) extrapolating the maximum throw along the whole fault in a*
875 *'boxcar-max' profile; and (iv) extrapolating throw along the fault by decreasing the maximum*
876 *throw linearly to the fault tips in a 'triangular' profile. Calculated earthquake $\geq M_w 5.1$*
877 *recurrence intervals are 420yrs, 465yrs, 262yrs and 524yrs for cases (i) – (iv) respectively. This*
878 *example shows that using simplified throw rate profiles can change calculated recurrence*
879 *intervals that are used to inform PSHA.*

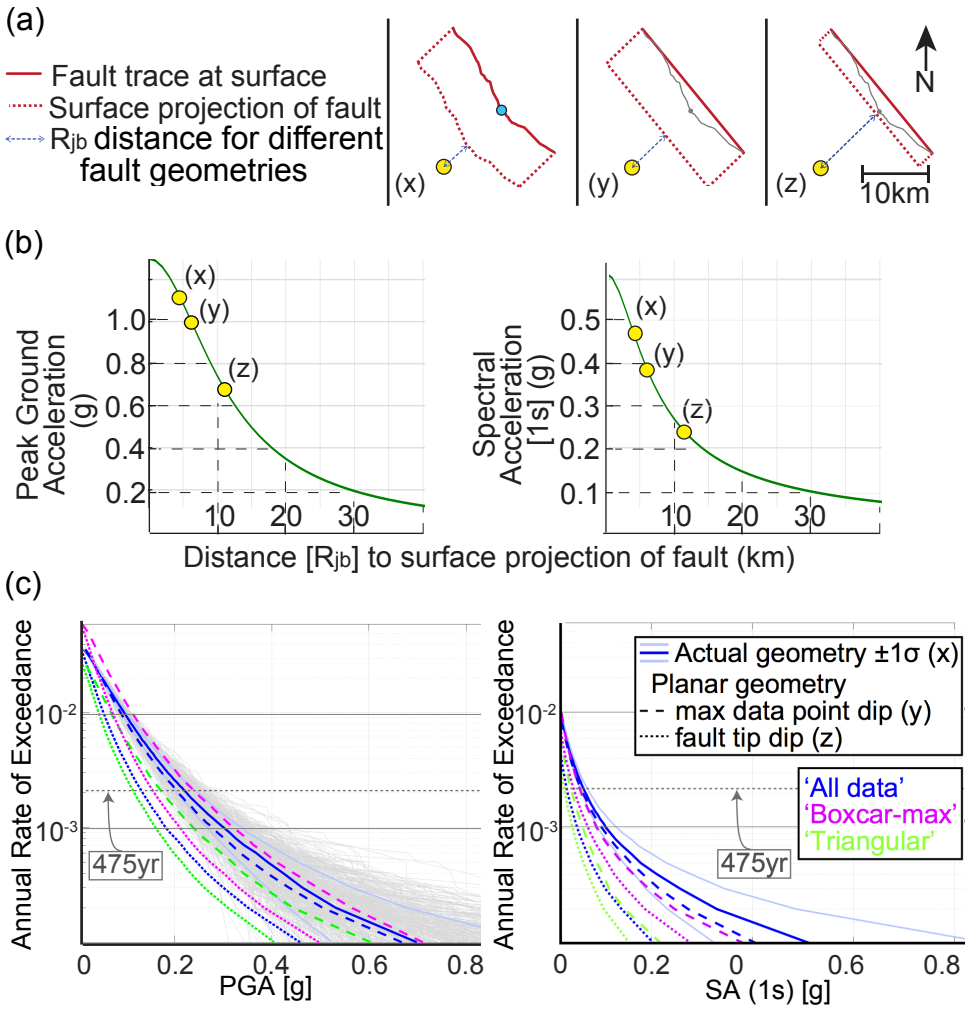

Figure 7: Effect of using simplified geometry and displacement rate profiles on annual rates of exceeding specified ground shaking intensities. The figure shows that ignoring fault bends and measured dips changes calculated shaking beyond 1σ uncertainty. (a) Maps show actual fault geometry (x) and surface projection of fault assuming the depth of the seismogenic layer is 15km and non-listric geometry with depth. The example site, Valle Massima, is shown as a yellow circle. The R_{jb} distance to the example site is 4.6km (x) (apparent dip of fault at (x) is 55°), but this distance is increased to 6.4km and 11.3km if the fault is simplified to having planar geometry between the tips with the dip projected from the maximum throw rate site (y) (55° apparent dip) and tip (z) (81° apparent dip) respectively. (b) The graphs show how the R_{jb}

distance affects peak ground acceleration and spectral acceleration with distances (x), (y) and (z) shown, using GMPEs from Bindi et el. (2011). (c) Annual rates of exceedance against peak ground acceleration (PGA) and spectral acceleration (SA) from earthquakes on the Pescasseroli fault at the given example site, Valle Massima. PGA and SA are calculated for the 'all data' throw profile for fault-to-site distances (R_{jb}) based on detailed fault geometry ((x), blue solid line, $\pm 1\sigma$ uncertainty shown with paler blue solid lines). Grey lines show each of the 500 simulation lines run for the PGA calculations. Ground shaking is further calculated using simplified planar fault geometries using a straight fault trace from tip-to-tip and fault dip projected from the maximum throw data site ((y), dashed line) and dip at the fault tip ((z), dotted line). The simplified fault geometry source-to-site distances are also combined with recurrence rates calculated for the 'boxcar-max' (pink lines) and 'triangular' (green lines) throw-profiles to show the combined effect of simplifying throw profiles and using simplified geometries. In this example, using a simplified throw rate profile and planar fault geometry gives lower values of calculated ground shaking intensities than using the actual values and therefore may underestimate the seismic hazard to a region or town.